Received: 7 July 2022 | Revised: 22 September 2022 | Accepted: 1 October 2022

DOI: 10.1111/jtxs.12729

RESEARCH ARTICLE

Journal of Texture Studies WILEY

Texture modulation of starch-based closed-cell foams using 3D printing: Deformation behavior beyond the elastic regime

Ahmed Raouf Fahmy[1] | Mario Jekle[2] | Thomas Becker[1]

[1]Technical University of Munich, TUM School of Life Sciences, Chair of Brewing and Beverage Technology, Research Group Cereal Technology and Process Engineering, Freising, Germany

[2]University of Hohenheim, Institute of Food Science and Biotechnology, Department of Plant-based Foods, Stuttgart, Germany

Correspondence
Ahmed Raouf Fahmy, Technical University of Munich, TUM School of Life Sciences, Chair of Brewing and Beverage Technology, Research Group Cereal Technology and Process Engineering, Freising, Germany.
Email: ahmed.fahmy@tum.de

Funding information
Deutsche Forschungsgemeinschaft, Grant/Award Number: 405072578

Abstract

3-dimensional printing is a novel processing method used for the design and manipulation of food textures. The systematic characterization and modulation of 3D printed food textures is imperative for the future design of sensory profiles using additive manufacturing. For 3D printed closed-cell food foams, the clarification of the deformation behavior in relation to design parameters is of interest for the processing of customized food textures. For this reason, we studied the deformation behavior of 3D printed and thermally stabilized closed-cell starch-based foams beyond the elastic regime. Periodic spherical bubble configurations at different porosity levels were used to modulate the deformation behavior of the printed foams. From a processing perspective, the integration of in-line thermal stabilization was used to eliminate post-processing and to control the moisture content of the starch-based system. Compression analysis combined with FEM simulations were performed to characterize the strain rate dependency of textural properties, the stress relaxation, and the foam's stress–strain behavior with respect to the design porosity and bubble distribution. Results showed that the stress relaxation is solely dependent on cell wall properties while different stress–strain regimes showed distinct dependencies on design parameters such as bubble size and distribution. Consequently, the precise control of the large deformation behavior of foods using 3D printing is challenging due to the superposition of structural and geometrical dependencies. Finally, through the presented approach, the structure-deformation relations of 3D printed closed-cell food structures are adequately described.

KEYWORDS
3D food printing, closed-cell foam, large-deformation behavior, texture design, texture modulation

1 | INTRODUCTION

Food texture design and modulation using 3-dimensional (3D) printing is based on the precise manipulation of food micro- and macro-structure. The adoption of 3D printing in the texture manipulation of foods is performed using a food layered manufacturing approach (FLM) where structures are constructed layer-by-layer. Using 3D geometrical models, 3D printing is used to construct complex structures and geometries by a layer-based deposition of the design geometrical and structural elements (Godoi et al., 2016; Lipton et al., 2010; Sun,

This article was published on AA publication on: 12 October 2022.

Peng, et al., 2015a; Sun, Zhou, et al., 2015b; Wegrzyn et al., 2012). While different 3D printing technological approaches are currently used for food processing, fused deposition modeling (FDM) is the most commonly utilized FLM technique which operates through material extrusion and deposition (ASTM-International, 2012). Moreover, FDM is applied in food printing applications such as in the modulation of food textures due to its compatibility with highly viscous food pastes (Chen et al., 2019; Derossi, Caporizzi, Paolillo, et al., 2020; Gholamipour-Shirazi et al., 2020; Liu & Zhang, 2021; Mantihal et al., 2020; Phuhongsung et al., 2020; Vancauwenberghe et al., 2018, 2019). Compared to the traditional processing of food textures, this approach enables the precise processing and fabrication of customized textures. In addition, FDM can facilitate the elucidation of textural dependencies and material-structure-processes relationships (Fahmy, Amann, et al., 2021; Fahmy, Becker, et al., 2021; Liu & Zhang, 2021; Pereira et al., 2021). By characterizing textural dependencies and deformation behavior through 3D printing, controlling the perception of food textures is possible and thus the design of sensory profiles is enabled.

The overall deformation behavior of cellular foods is defined by the base material properties, the relative density, the foam's cellular structure, and the applied structuring process. Moreover, the deformation behavior influences the mechanical and textural properties of cellular food foams. Prior to the structuring and post-processing, the food microstructure is determined through the raw materials' chemical structure and interactions as well as through the pre-processing conditions. Furthermore, the macrostructure is initially resolved and affected by the microstructure. Textures of cereals and food foams in general are scientifically defined as the manifestation and interaction of mechanical, structural, and surface properties (Szczesniak, 2002). The mechanical properties including textures of starch-based foams influences both the deformation and mastication behaviors of such cellular structures and thus affecting their sensory profile (Wang et al., 2011). The mastication process, which is correlated to the deformation behavior, influences the foam's nutritional characteristics (Takahashi et al., 2009). Therefore, controlling and designing the textural perception of starch-based cellular foams using 3D printing can be performed by the control over the base material's properties and the modulation of the foam's micro- and macro-structure.

Considering the manipulation of the cellular structure using 3D printing, many studies focus on the modulation of textures using multiple infill variations and relative densities (Derossi, Caporizzi, Oral, et al., 2020; Derossi, Caporizzi, Paolillo, et al., 2020; Lille et al., 2020; Liu et al., 2018; Pereira et al., 2021; Phuhongsung et al., 2020; Piovesan et al., 2020; Varghese et al., 2020; Zhao et al., 2021; Zhu et al., 2021). Most studies focus on the modulation and the characterization of the deformation behavior in the elastic regime. However, few articles highlight the mechanical and sensory behavior of 3D printed food structures beyond the textural properties in the elastic regime (Jonkers et al., 2020; Lille et al., 2020; Shahbazi et al., 2021a, 2021b). The study performed by Lille et al. modulated the fracture force of periodic open-cell structures (describing the cutting force needed to break the sample) by varying the 3D printed food formulation (Lille et al., 2020). Modulation of the fracture force was not performed by varying the design parameters of the cellular structures such as the design porosity and pore distribution. Moreover, the authors attempted to correlate the analytical findings with sensory analysis with respect to the printed food formulation. Jonkers et al. presented a modeling approach for predicting the full stress strain behavior of food structures printed using selective laser sintering (Jonkers et al., 2020). For the sintered dense food structures, the authors showed a 3D constitutive model which incorporates inelastic deformation and allows for high non-linearity. Furthermore, the study presented by Shahbazi et al. showed a new approach for the structuring of personalized food through the application of 3D printing of casein-based Pickering emulsion (Shahbazi et al., 2021a, 2021b). The authors studied the tribological behavior of the structured analogs through oral tribology and rheometry measurements. To conclude, extending the characterization and modulation of the structure-dependent deformation behavior in the large-strain non-linear regime in relation to the cellular design properties is essential for designing variable texture profiles through 3D printing. This importance arises as the larger-strain behavior is the main determinant of the cellular food's mastication performance and sensory perception.

This study was performed on three 3D printed closed-cell foam configurations using spherical bubbles in simple, body-centered, and face-centered cubic designs. The foam configurations were 3D printed using a starch-based material system composed of hydrated wheat starch and soy protein. The three starch-based foam configurations were printed using a cubic design of 8 cm^3 in volume, irrespective of the foam porosity. Moreover, the simple cubic design consisted of eight corner bubbles and the body-centered design consisted of eight corner bubbles with an additional bubble located at the center of the printed cubic structure. Furthermore, the face-centered design incorporated a total of 14 bubbles consisting of eight corner bubbles and six bubbles located at the center of each cube face. For this investigation, design and heating parameters were modulated for 3D printing of closed-cell structures to achieve pre-determined hardness levels (Fahmy et al., 2022). A 3D printing method for texture creation was used incorporating in-line NIR heating for moisture control and for modulating the base material's Youngs' modulus (Fahmy, Amann, et al., 2021). Measurements that were performed using analytical texture profile analysis (TPA) were compared with finite element (FEM) simulations to verify the precision of the printed structures. Also, the comparison between TPA analyses and FEM simulations was performed to investigate and eliminate any inherited geometrical defects during the printing process which might affect the textural and mechanical response during loading. First, the strain rate dependency of the textural properties was investigated at variable applied deformation rates. Second, the viscoelastic response of the 3D printed cellular structures was investigated using stress relaxation measurements with the application of the Peleg-Normand model (Peleg & Normand, 1983). Third, the large-strain deformation behavior was investigated using compressive analysis with respect to cellular design, relative density, and base material's Young's modulus. The stress–strain behavior including yielding, plateau, and densification

TABLE 1 Wheat starch-soy protein material system composition used for 3D printing of closed-cell structures

	Wheat starch		Protein		Distilled water	
Material system	Mass ratio (%)	Amount (g)	Mass ratio (%)	Amount (g)	Mass ratio (%)	Amount (g)
SPI	42.50	42.50	7.50	7.50	50.00	50.00

regimes of the 3D printed cellular structures were characterized using a phenomenological foam model (PFM) presented by Goga et al. which applies a macroscopic-level modeling approach (Goga & Hučko, 2016). Finally, structure-deformation relations were obtained with respect to the base material's properties, applied heating, and cellular design configuration and porosity.

2 | MATERIALS AND METHODS

2.1 | Raw materials

One material system composed of hydrated wheat starch and soy protein isolate was used for the 3D printing of the different closed-cell foam configurations. The soy protein isolate was purchased from Bulk Powders (Colchester, United Kingdom). The wheat starch was provided by Kröner-Stärke GmbH (Ibbenbüren, Germany). The protein and moisture contents were determined according to the methods of the American Association of Cereal Chemists international (AACCi) 46–16 and 44–01, respectively. The wheat starch had a moisture content of 13.98 ± 0.17% ($n = 3$) and a protein content of 0.27% ($n = 1$; dry mass). The soy protein isolate had a moisture content of 6.79 ± 0.21% ($n = 3$) and a protein content of 88.75% ($n = 1$; dry mass). The material analyses were performed in triplicates.

2.2 | Material preparation

To modulate and characterize the texture, deformation, and stress–strain behavior of 3D printed closed-cell structures, one starch-based mixture was used. Measurement of the printing quality and geometrical stability of the starch-based material was performed using an approach based on in-line camera-based analysis and rheological characterization which was proposed in earlier articles (Fahmy et al., 2019, 2020). The specific choice of the material formulation was based on the characterization of printing quality and performance presented in our previous study which presents an approach for designing closed-cell food foams for achieving specific hardness levels (Fahmy et al., 2022). In this study, the same material formulation is used to investigate the strain rate dependency of the textural properties for the purpose of textural modulation using 3D printing. Also, to investigate the viscoelastic response and large-strain deformation behavior and their dependency of the foam's structure as well as the foam's relative density. Hereby, we used a mixture of hydrated wheat starch and soy protein isolate (SPI). For showing a comparable composition to wheat flour constituents, the starch to protein ratio was kept to 85:15. The hydration level of the dry components was 50% of the total mass ratio (Fahmy et al., 2022). Table 1 shows the mixture composition for the used material system.

For the preparation of the starch-based mixture, a z-type kneader was used at 63 rpm. First, a pre-mixing step of 1 min was performed to mix the dry ingredients. Second, the water was added, and the mixture was kneaded for 10 min at a room temperature of 18 ± 2°C. Following the kneading process, the mixture was removed, placed directly in the printing cartridges, covered using PARAFILM (Bemis Company Inc., Wisconsin), and rested for 15 min at room temperature until the preparation of the used progressive cavity pump (PCP) extruder is completed. As the PCP extruder consists of a stator and a stepper controlled rotor, the preparation includes the assembly of both within the extruder's housing forming the progressing cavity. Directly after assembling the main extruder's components, the material-containing cartridge is attached. The starch-based material was prepared in triplicates. Furthermore, for each material preparation, 3D printing, and measurements were performed in triplicates.

2.3 | 3D printing setup and designs

For printing the starch-based closed-cell structures, an X400 V3 3D printer (German RepRap GmbH, Feldkirchen, Germany) was used. For generating the machine G-code files, simplify3D slicing software (simplify3D, Ohio) was used. All printing experiments were performed using a conical nozzle of 0.84 mm in diameter, at a printing speed of 10 mm/s, and at an extrusion width\height of 0.84 mm. A detailed description of the printing setup and the pre-printing calibration process was mentioned in our previous study which investigates the printing quality of starch-base material systems using a camera-based morphological approach (Fahmy et al., 2020). For the transport and deposition of the material, a progressing cavity pump (PCP) was used in all printing experiments (ViscoTec GmbH, Töging, Germany). The PCP (Vipro-head3) has a theoretical flow rate range of 0.3–3.3 ml/min. The flow rate of the pump depends on the printing settings as well as the rheological-viscoelastic properties and flow behavior of the printed material. Moreover, a near-infrared (NIR) spot heater (Optron GmbH, Garbsen, Germany) was used for the in-line thermal stabilization of the printed structures. The variable output 150 W spot heater is equipped with a NIR-emitter that has a peak wavelength of approximately ~0.98 μm. Through a control unit that was used as an interface between the heater and the 3D printer, the heating power is controlled through pulse width modulation (PWM). To control the heating power, the PWM was mapped to a 10 V DC output of the 3D printer. Furthermore, all printed structures were printedat room temperature

of approx. 21 ± 2.0°C and then thermally stabilized in a layer-based approach using the NIR spot heater (Fahmy, Amann, et al., 2021). Finally, a detailed description of the thermal stabilization process can be found in section 2.5.

To modulate and characterize the textural properties and the stress–strain behavior of 3D printed starch-based structures, three closed-cell foam designs were used. For generalizing the results of all analyses, all designs which were digitally constructed, and 3D printed are considered as unit-cells that can be assembled longitudinally and transversely to obtain larger closed-cell structures (Fahmy et al., 2022). For all designs, a cubic structure with a volume of 8 cm^3, a surface area of 400 mm^2 and a height of 20 mm was chosen. The three closed-cell designs were composed of spherical bubbles arranged in point-lattice configurations which are simple, body-centered, and face-centered cubic designs (Fahmy et al., 2022). The simple cubic SC design is composed of eight bubbles while the body-centered BCC and the face-centered FCC designs are composed of nine and 14 bubbles respectively. The SC design incorporates the eight bubbles on the corners of the cubic lattice. The BCC design incorporates eight corner bubbles with a central bubble located in the spatial center of the cubic structure. Furthermore, the FCC design also incorporates the eight corner bubbles like the SC and BCC designs with the addition of six bubbles located at the centers of the cubic structure's faces. For all designs, the distance between the corner bubbles was chosen to be 10 mm throughout the 3D printing trials. All cellular configurations were 3D printed at five porosity levels of 0, 2.5, 5, 10, and 15% while keeping the printed volume constant. To illustrate, the printed designs were printed at the same volume and porosity, which leads to different bubble sizes due to the difference in bubble quantity between the three configurations. Finally, the full parametric modeling of the printed designs was presented in our previous study concerning the hardness targeted design of 3D printed closed-cell foams (Fahmy et al., 2022).

2.4 | Texture profile analysis and mechanical characterizations

To characterize the deformation behavior of all printed closed-cell structures, a TA. TX. plus Texture Analyzer (Stable Micro Systems Ltd, Godalming, UK) was used. TPA tests were performed using a 50 Kg measuring cell. To apply the compression analysis on all printed structures, a 50 mm cylindrical probe was used. All measurements were conducted at room temperature of 18 ± 2.0°C. To characterize the textural properties of the closed-cell structures and their strain rate dependency, double compression tests were applied at 10% deformation, a trigger force of 0.05 N, and at variable strain rates. The double compression tests were performed at five strain rate levels which are 0.5, 1.25, 2.5, 3.75, and 5/s. To characterize the viscoelastic response of the closed-cell foams, stress relaxation measurements were performed at a strain of 0.5%. The strain was applied and kept constant for 30 s, where the force profile was measured as a function of time. For obtaining the stress–strain behavior of the closed-cell structures beyond the elastic regime, the printed structures were compressed to 80% of their original height to identify the yielding, plateau, and densification regimes. The developed force profiles were analyzed with respect to the deformation distance and time. Due to the large applied strain, the deformed cross-sectional area is required for measuring the true stress. As the in-line measurement of the deformed cross-sectional area was not possible during this study, the engineering stress was used instead of the true stress. Finally, all compression measurements were performed in triplicates.

To compute the engineering Young's modulus E_{eng} from the double compression test, the engineering stress σ_{eng} and strain ε_{eng} were obtained from the measured force-distance curves using the following equation: $\sigma_{eng}/\varepsilon_{eng} = ((F/A)/(\Delta H/H))$ (2.1), where the F is the measured force (N), A is the sample cross-sectional area (m^2), H is the sample height (m), and the ΔH is the lateral deformation (m) (Attenburrow et al., 1989; Beer et al., 2011; Roylance, 1996). From the initial engineering stress–strain linear behavior, the engineering Young's modulus E_{eng} was obtained using a linear regression with a regression coefficient higher than 0.95. The textural properties were characterized from the force-displacement curve of the double compression tests. The following attributes were determined as a function of the closed-cell bubble configuration, porosity, and the applied strain rate: hardness (H) which was defined as the first compression cycle's peak force, cohesiveness (C) which was defined as the area ratio of the second to the first compression, and resilience (R) which was defined as the ratio of energies equivalent to the ratio of decompression and compression cycles (Peleg, 2019; Szczesniak, 1963).

For elucidating the stress relaxation behavior of the printed closed-cell foam configurations, the viscoelastic response was characterized using the Peleg-Normand model (Peleg & Normand, 1983). Through the normalized relaxation curves presented by the Maxwell model for stress relaxation, the stress relaxation curves were normalized in the form of: $(\sigma_{eng\_0} * t)/(\sigma_{eng\_0} - \sigma(t)) = k_1 + k_2 t$ (2.2), where σ_{eng_0} is the initial stress (Pa), $\sigma(t)$ is the instantaneous decay stress (Pa) with respect to time t (s). The k_1 (s) and k_2 are the Peleg-Normand constants. They represent the intercept and slope of the regression obtained by the normalized stress with respect to time. To further illustrate, the constant k_1 quantifies the initial rate of decay of the developed compressive stress (described as the initial rate of relaxation). Moreover, the constant k_2 describes the extent of relaxation. Which quantifies the residual stress as time tends to infinity. In this study, another calculated parameter %SR (%) was used to characterize the stress relaxation behavior of the printed closed-cell configurations (Hatcher et al., 2008). The parameter %SR provides a comparative measurement of the viscoelastic behavior at an arbitrary time: $\%SR = \left(\sigma_{eng\_0} - \sigma_{eng\_t}/\sigma_{eng\_0}\right) * 100$ (2.3), where σ_{eng_0} is the initial stress (Pa) and σ_{eng_t} is the stress at an arbitrary time t (Pa). Furthermore, % SR = 100% for an ideal viscous behavior presented by an ideal liquid while for an ideal elastic behavior of an elastic solid %SR = 0%. For this study, the %SR was calculated at time t = 20 s (Figure 1).

To characterize the compressive stress–strain behavior of the 3D printed closed-cell foam configurations, a phenomenological foam model (PFM) presented by Goga et al. was used (Goga & Hučko, 2016). Phenomenological foam models are developed using a macroscopic level modeling approach. For modeling at the

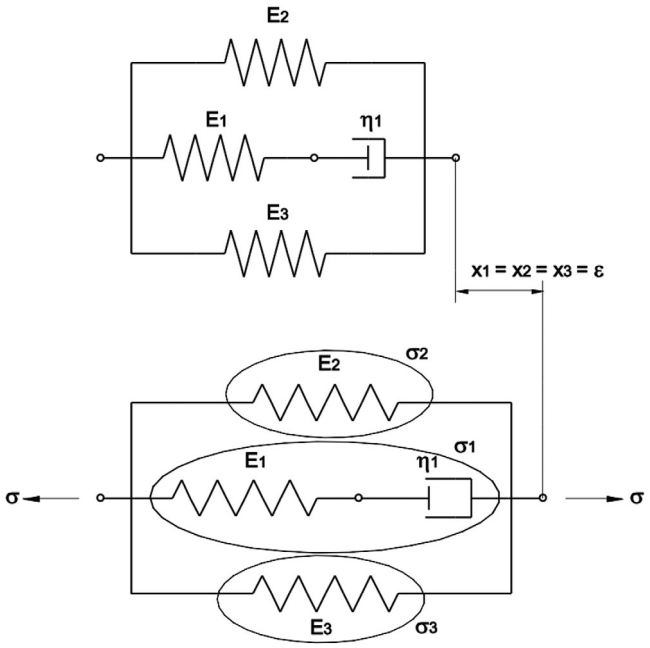

FIGURE 1 Goga PFM rheological model for cellular solids (Goga & Hučko, 2016). The serial Maxwell model (spring E_1 and damper η_1) represents the linear elastic region of the stress–strain behavior. The strain locking (plateau) and densification regimes are modeled as springs (E_2 and E_3, respectively) in parallel configuration to the Maxwell model

macroscopic level, the foam's macroscopic behavior can be elucidated by a set of constitutive equations where the foam is assumed to be a continuum (Avalle et al., 2007; Goga & Hučko, 2016; Liu & Subhash, 2004). This approach focuses on describing the deformation behavior (shape of compressive stress–strain) using appropriate mathematical descriptors during the establishment of the constitutive equations (Goga & Hučko, 2016). The PFM presented by Goga et al. (Goga PFM) is applicable for all cellular solids having the same characteristic response during compression (like foams and honeycombs) which is characterized by three regimes: a linear elastic regime, a stress plateau and a densification or strain locking region (Gibson, 1989; Gibson & Ashby, 1999). The linear elastic regime corresponds to the elastic bending of the cell walls while the plateau and strain locking (densification) regimes correspond to the plastic yielding (or elastic buckling depending on the constitutive foam material) and to the collapse of cells, respectively. The Goga PFM models each region separately using a rheological model which determines the influence of all parameters in relation to the compressive stress–strain behavior. The linear region is modeled using a Maxwell model which consists of a linear spring E_1 and a viscous damper η_1 in series. For the plateau region, a linear spring E_2 is connected in parallel to the Maxwell model. Finally, considering the densification or strain locking region, it is characterized by a strong non-linear increase behavior which is modeled as a non-linear spring E_3 in parallel to the Maxwell model. Regarding the relationship between the resultant stresses and strain(Goga & Hučko, 2016), the Goga model can be denoted as: $\sigma(\epsilon) = e^{-\left(E_1/\eta_1\right)\epsilon}\left(-1+e^{-\left(E_1/\eta_1\right)\epsilon}\right)\eta_1 + \left(E_2+\gamma(1-e^{\epsilon})^h\right)\epsilon$ (2.4). The presented model contains five parameters (E_1, η_1, E_2, γ, and h) which represents stresses and all of them are positive except the E_2 which represents the slope direction of the plateau regime. The parameter h is a dimensionless parameter which is usually four or six (Goga & Hučko, 2016). For this study, the young's modulus was characterized using the double compression tests. Thus, this study focuses on characterizing and comparing the damping coefficient η which corresponds to the yielding behavior of the foam, the plateau stiffness E_p which represents the inclination, and the densification coefficient γ. The objective is to characterize the dependency and behavior of such parameters in relation to the modulation of the base material's properties, the relative density or porosity, and the bubble configuration.

2.5 | In-line near infrared NIR heating

An in-line thermal stabilization approach was used for heat treating the printed closed-cell configurations during the 3D printing process. A NIR spot heater composed of one NIR lamp and a focusing reflector was used. A detailed description of the heater properties and interface was mentioned in section 2.3. The spot heater is equipped with a lens which resulted in a 6 mm spot diameter at a focal length of 17 mm. For all printing trials, the heat treatment was applied at the focal length of 17 mm.

A layer-based heating approach was adopted for the thermal stabilization of the printed structures (Fahmy, Amann, et al., 2021). After 3D printing of one layer, the heating process is applied then the printing of the subsequent layer is performed. As mentioned in section 2.3, the surface area of the printed structures is 400 mm^2 where the effective surface area of the NIR spot is smaller which is approx. ~113 mm^2. For this reason and to uniformly heat the surface area of the printed structures, a square function for the movement of the NIR spot was applied (Fahmy, Amann, et al., 2021). The square function has a period which is equivalent to the spot diameter, but with a phase shift of $-45°$. The function's period was chosen so that the application of heat is performed once per surface location. For all printed structures, the heating power was kept constant at 32%, regardless of the design porosity or bubble configuration. On the other hand, the movement speed of the heating spot was adjusted depending on the structure porosity to maintain the same moisture content for all printed structures. The moisture content of the printed and thermally treated structures was measured according to the AACCi 44–01 standard.

2.6 | FEM modeling and simulation

ANSYS Workbench 2020 R1 (ANSYS Inc., Pennsylvania) was used to simulate the developed stresses, deformation behavior and hardness of the designed closed-cell configurations. FEM simulations of the cellular designs were compared to TPA results to justify the precision of the printed structures (Fahmy et al., 2022). In addition, the simulations were used to highlight the differences in the developed stresses between the different bubble configurations. To simulate the

designed structures, the models were imported to the ANSYS Design-Modeler as a Parasolid extension format. For obtaining the structural deformation and hardness, a transient structural analysis was performed. Prior to the transient mechanical simulations, a mesh sensitivity analysis (results not shown) was performed on the designed unit cell structures to determine the element size and count. The analyses were performed using a tetrahedron simplex geometry where the element size and count were chosen after the convergence of the model's hardness value. For a designed model volume of 8 cm^3, the discretization was performed using a maximum mesh size of 800 μm that resulted in more than 130,000 tetrahedron elements. Regarding the transient solution setup and boundary conditions, the load was applied on the top surface of the structure as it was considered as a displacement boundary. Moreover, as an accurate representation of the TPA compression analysis, the bottom surface of the structure was taken as a fixed boundary. A 1 mm/s vertical velocity was set for the top surface or the displacement boundary while the double compression deformation was set to 10%. A total compression duration of 20 s was applied, and the models were solved using a time step of 0.5 s. The Young's modulus and density that were applied in the linear elastic model were measured using the TPA using the bulk material (without the inclusion of porosity). The measurements were performed under quasi-static conditions at room temperature of 18 ± 2.0°C and at a low strain rate of 0.025/s. The base material's Young's modulus was applied depending on the attenuation of in-line thermal stabilization speed which is clarified in section 3 (Fahmy et al., 2022). For all simulated structures, a low Poisson's ratio of 0.1 was applied to the material model. Only the linear elasticity was considered for all simulations while viscoelasticity was not considered. The transient mechanical simulations were performed using a 64-bit, 3.00 GHz Intel Core i7-9700F CPU, 32 Gb RAM, NVIDIA GeForce RTX 2060 super GPU, and Windows 10 Professional computer.

2.7 | Data analysis

The computation of equations, data analysis and regression fitting for the simulated and the mechanically tested closed-cell foams were performed using MATLAB R2020a (MathWorks, Massachusetts) and OriginPro 2020 (OriginLab Corporation, Massachusetts). Furthermore, for the regression fitting of all obtained parameters, both linear and exponential regressions were fitted and the coefficients of determination R^2 were compared. The behavior of all obtained parameters was identified by either one of the mentioned regressions depending on a higher coefficient of determination.

3 | RESULTS AND DISCUSSION

3.1 | Modulation of deformation and stress–strain behaviors

The mechanical and deformation behavior of processed elastomeric cellular foams is highly dependent on the base material properties, the geometry, and the foam's relative density (Avalle et al., 2007; Gibson, 1989; Gibson & Ashby, 1999; Jang et al., 2008; Zghal et al., 2002). Ensuring a high accuracy of the printed starch-based cellular configurations is of outmost importance for eliminating viscoelastic induced defects during printing which lead to geometrical and thus textural deviations from the designed structures. And thus, high precision is required during printing to ensure comparable and even equivalent geometry and porosity to the designed closed-cell bubble configurations. For this reason, two hierarchical stages of quality assessment were performed.

The two quality characterization stages include the printing quality characterization of the base material and the accuracy assessment of the printed porosities. First, to assess the printability of the used starch-based material, a camera-based morphological approach was used which we described in details in our previous studies (Fahmy et al., 2019, 2020). This method assesses the printability by comparing geometrical dimensions of printed structures to design parameters. Also, the method assesses key defect parameters with respect to the viscoelastic behavior of cereal- and starch-based materials. Using the mentioned approach, the printing quality of the wheat starch-soy protein (SPI) material (Table 1) used for printing the closed-cell bubble configurations was compared to other starch-based material systems in our previous study (Fahmy et al., 2022). The used SPI material formulation (Table 1), compared to the other characterized material formulations, showed in a previous study the highest geometrical accuracy and stability (Fahmy et al., 2022). Second, to assess the accuracy of the printed porosities, a FEM simulation approach was used instead of x-ray microtomography (Fahmy et al., 2022). A comparison between the hardness obtained from TPA analyses and FEM simulations is performed where comparable hardness results indicate comparable porosity levels between the designed and printed structures.

Prior to investigating the textural, deformation, and stress–strain behavior of the three designed closed-cell configurations, the hardness was measured using a double compression TPA test and compared to FEM simulations. The TPA measurements and FEM simulations were performed and compared at specific designed porosity-dependent hardness values. In our previous study regarding hardness-targeted design of 3D printed structures, we developed an equation (hardness-targeted PFM) which enables the design of printing parameters with respect to specified hardness values: $H_{unit\ cell} = -1.23 + \left(8.24 * 10^{-5}\right) A_{unit\ cell} + \left(7.1 * 10^{-4}\right) E + \left(1.15 * 10^{-8}\right) A^2_{unit\ cell} + \left(1.2 * 10^{-6}\right) EPA_{unit\ cell}$ (*3.1*), where $H_{unit\ cell}$ is the selected hardness for the printed structure (N), $A_{unit\ cell}$ is the effective compression area (mm^2), P is the design porosity (%), and the E is the base material's young's modulus (kPa) (Fahmy et al., 2022). To determine the accuracy of the printed porosities through comparing the hardness obtained from TPA measurements and FEM simulations, shown in Table 2, structures which exhibit a decrease in hardness with the increase in porosity were selected using equation 3.1. As mentioned in section 2.3, the printed configurations were designed with a specific constant surface area $A_{unit\ cell}$ of 400 mm^2 and five levels of porosity which are 0, 2.5, 5, 10, and 15%. Therefore, after the computation of equation 3.1, the

TABLE 2 Base material's Young's modulus computed according to equation 3.1 with the design parameters

Porosity P	Surface area $A_{\text{unit cell}}$	Selected hardness $H_{\text{unit cell}}$	Calculated material Young's modulus E
(%)	(mm^2)	(N)	(kPa) at $P = 0\%$
0	400	14	364.2
2.5	400	12	315.4
5	400	10	249.8
10	400	7	216.5
15	400	4	148.9

base-material's Young's modulus required modulation to achieve the designed hardness levels as shown in Table 2.

For all printed porosities of the designed point lattice bubble configurations, the moisture content was kept constant and the Young's modulus was modulated using a porosity dependent equation for moisture attenuation using variable heating speeds which we presented in our previous study ($R^2 = 0.95$): $v = \frac{P-82.65}{-6.36}$ (3.2), where v is the heater movement speed (mm/s) and P is the porosity of the printed structure (%) (Fahmy et al., 2022). For obtaining the mentioned equation, structures with constant design porosity were printed and the heating speed was varied between 9 and 15 mm/s with a step size of 2 mm/s. The analyzed moisture content of the printed and heated structures showed a linear increase with respect to the increase in heating speed. A linear regression was fitted to obtain the relation between the applied heating speed and the resultant moisture content. The dependency between the resultant moisture content and the applied heating speed was shown in our previous article concerning the hardness targeted design of 3D printed closed-cell foams (Fahmy et al., 2022). A change in heating speed of $v = 1.06$ mm/s per 1% change in moisture content was observed from the obtained regression. Then, the moisture content was characterized with respect variable porosities at a constant heating speed. Furthermore, by obtaining both relations and through simple substitution, the shown porosity dependent equation for the attenuation of the moisture content was formulated (Fahmy et al., 2022). For an average moisture content of 47.79 ± 0.2% for all printed porosities, the heating speed was modulated, and the Young's moduli were characterized under quasi-static conditions using double compression tests in the elastic regime (section 2.4). As shown in our previous study (Fahmy et al., 2022), an exponential decay dependency of the young's modulus on the heating speed was observed. Moreover, a heating speed-dependent Young's modulus modulation function was obtained ($R^2 = 0.98$): $E = \left(1.31 * 10^{12}\right) e^{-v_{35.7}} + 66.37$ (3.3), where E is the modulated young's modulus (kPa). From equation 3.3, the heating speeds were calculated and applied during the in-line heating of the printed structures. The calculated heating speeds were used to modulate the base material's Young's modulus.

For simulating the compressive behavior of the closed-cell foam structures, the calculated Young's moduli were used in the FEM model, depending on the simulated porosity. As shown in Figure 2, the hardness of the printed configurations at the designed porosities were characterized and compared to the FEM simulations. From the

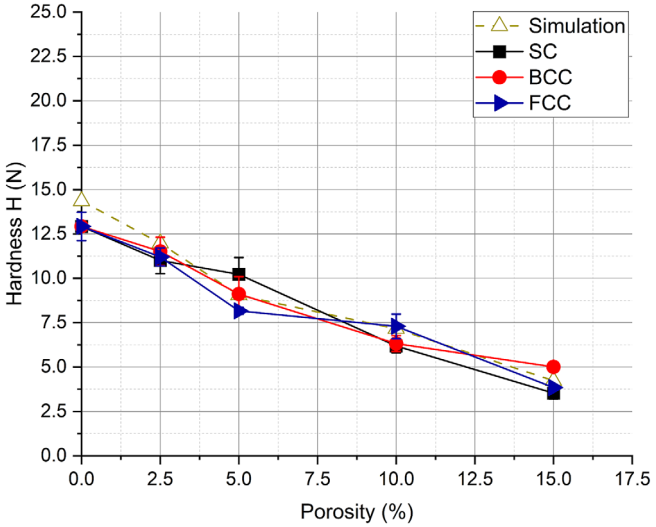

FIGURE 2 TPA measurements and FEM simulation of hardness of the 3D printed closed-cell configurations at the selected porosity levels (STD $n = 3$). Simulations of the SC, BCC and FCC configurations resulted in an equivalent hardness regression with respect to the design porosity. Thus, the presented simulation regression represents the simulation of the three closed-cell configurations

obtained results, there was no clear dependency of the hardness on the simulated or measured configuration but rather only a dependency on the porosity (Fahmy et al., 2022). This is supported by literature where the elastic deformation of cellular structures depends on the based material constituents and properties as well as the foam's relative density (Gibson, 1989; Gibson & Ashby, 1999). Both simulated and 3D printed structures showed the same decrease behavior with respect to the increase in porosity. By comparing the FEM hardness values with the characterized 3D printed structures, the average deviations for all porosity levels of the SC, BCC, and FCC were observed as 9.7 ± 3.3%, 5.5 ± 3.0%, and 6.93 ± 3.4%, respectively. The calculated deviations between simulation and printing can be related to the occurring structural defects due to heating and printing uncertainties (Fahmy et al., 2022). The inherited geometrical defects can be contributed to in-accuracies in the target porosities or in the printed volume. Finally, the relatively low deviations between 3D printing and FEM simulations show moderate accuracy in printing the designed closed-cell configurations at different porosity levels.

Elastomeric cellular foams are usually non-linear viscoelastic materials which exhibits high static and dynamic linear and viscoelastic behaviors (Alzoubi et al., 2014; Avalle et al., 2007; Gao et al., 2018; Goga & Hučko, 2016; Wu et al., 2012; Zghal et al., 2002). Moreover, most studies concerning texture modulation of 3D printed food foams do not extend their textural characterization at different strain rates (Derossi, Caporizzi, Paolillo, et al., 2020; Liu & Zhang, 2021; Pereira et al., 2021; Piovesan et al., 2020; Varghese et al., 2020). Thus, double compression tests were performed at five strain rate levels in the elastic regime to elucidate the strain rate dependent behavior of the 3D printed structures and its dependency on the structural configuration as well as the base material's young's modulus. The tests were performed for the three designed bubble configurations (SC, BCC, and FCC) where the foam's engineering Young's modulus, hardness, cohesiveness, and resilience were characterized at 10% deformation. Furthermore, to characterize the textural properties and their strain rate dependency, the tests were applied at five strain levels of 0.5, 1.25, 2.5, 3.75, and 5/s.

Figure 3 shows the porosity and strain rate dependency of the hardness and engineering Young's modulus of the BCC closed-cell configuration. Concerning the dependency of hardness and Young's modulus on the printed porosity at the strain rate level of 0.5/s, the SC, BCC, and FCC configurations showed the same decrease behavior and absolute values as verified previously using FEM simulations, as

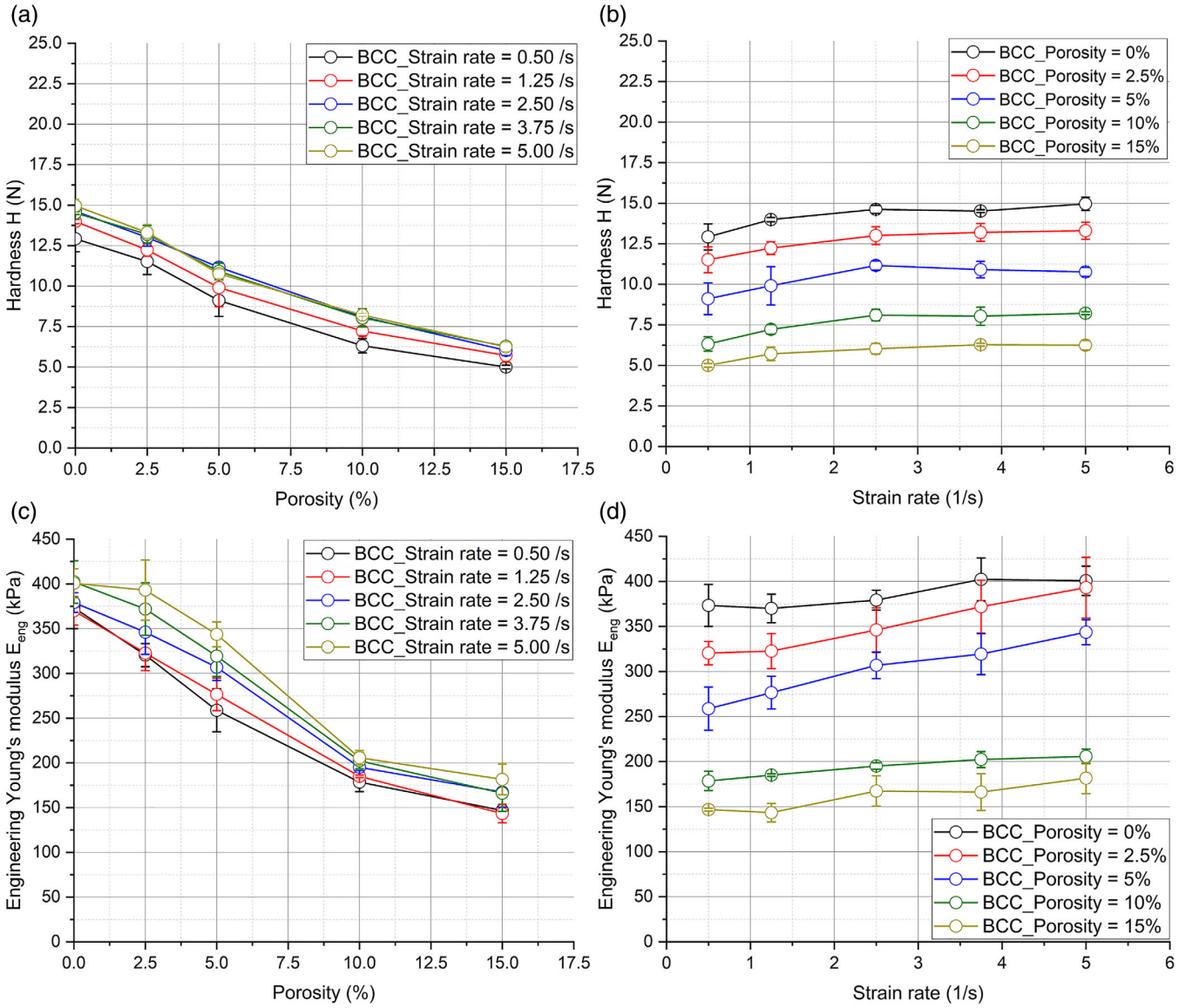

FIGURE 3 TPA measurement of porosity and strain rate dependency of the hardness and engineering Young's modulus of the body-centered cubic (BCC) bubble configuration (STD $n = 3$): (a) hardness behavior with respect to increasing porosity at different applied strain rates; (b) hardness behavior with respect to increasing strain rate at the designed porosity levels; (c) behavior of Young's modulus with respect to increasing porosity at different applied strain rates; (d) behavior of Young's modulus with respect to increasing strain rate at the designed porosity levels

illustrated in Figure 2. As shown in Figure 3a, considering the BCC configuration, an increase in the hardness decay at the different porosities was observed with respect to the applied strain rate. This can be clearly observed when plotting the hardness against the strain rate of the different printed porosities, as presented in Figure 3b. A linear increase was observed where the hardness increased from 12.9 ± 0.8 N at 0.5/s to 14.9 ± 0.4 N at 5/s for the 0% porosity while the hardness increased from 5.0 ± 0.2 N at 0.5/s to 6.3 ± 0.3 N at 5/s for the 15% porosity. The results indicate an increase of approx. ~15.5% in the hardness of the base material (0% porosity) with respect to an increase of 10 folds in the applied strain rate of deformation. At the same time, an increase of 26% was observed for the hardness of the BCC configuration at 15% porosity with respect to the same increase in the applied strain rate of deformation. Figure 3c shows a linear decrease behavior of the engineering Young's modulus with respect to the design porosity of printed closed-closed cell foams. A similar linear decrease behavior was reported by Piovesan et al. while the Young's modulus was characterized on open-cell honey comb structures (Piovesan et al., 2020). The comparable Young's modulus behavior between open- and closed-cell designs shows the independency of its decrease behavior on the pore geometry and distribution. In addition, the same behavior was observed for the SC and FCC configurations (results not shown). This eliminates the dependency of the strain rate response of hardness and engineering Young's modulus with respect to the printed configuration. As the different printed porosities are subjected to different heating speeds to modulate the base material's Young's modulus, the strain rate dependency of hardness of the base material was investigated with respect to the applied heating speed. A linear increase was observed where the hardness increased from 12.9 ± 0.8 N at 0.5/s to 14.9 ± 0.4 N at 5/s for the 13.0 mm/s heating speed corresponding to the base material of the 0% porosity while the hardness increased from 8.2 ± 0.1 N at 0.5/s to 9.8 ± 0.6 N at 5/s for the 15.4 mm/s heating speed corresponding to the base material of the 15% porosity. This indicates the same increase of approx. ~15.5% for the base material while an increase of only ~19.5% for the heating speed (15.4 mm/s) that is used for printing the structures with 15% porosity. Therefore, independent of the printed configuration, the strain rate response of hardness is dependent on the base material's mechanical properties of the cell walls superimposed by the response of the closed cells. On the contrary, the resilience and cohesiveness was observed to be dependent only on the applied strain rate where the value and increase response remained unchanged with respect to the applied heating speed, the closed-cell configuration, and the porosity. This independence of the applied heating speed can indicate that principal physiochemical transitions within the constituent components did not occur to alter the material's response Figure 4.

For characterizing the viscoelastic response of the closed-cell foam configurations, the stress relaxation spectra of the structures were investigated. The printed structures were compressed at a constant strain of 0.5% for 30 s. The developed stress profiles were recorded with respect to the relaxation time. The engineering stress-time responses were analyzed using the Peleg-Normand stress relaxation model (R^2 > 0.95) as presented previously in section 2.4. The normalized stress and model parameters were computed and compared with respect to the applied heating speed corresponding to the Young's modulus modulation of the base material. This comparison was performed to investigate the dependency of the viscoelastic response with respect to the base material's state depending on the applied NIR thermal energy. Also, the model parameters were computed and compared in relation to the printed closed-cell foam configurations at variable porosities. Consequently, the dependency of the stress relaxation response was obtained as a function of porosity and bubble lattice configuration.

Considering the stress relaxation response with respect to the applied NIR speed, the normalized stress profiles show a decrease in the linear growth with the increase in NIR heating speed, as shown in Figure 5. This indicates a decrease in the linear growth of the normalized stress with respect to the decrease in the Young's modulus of the base material (Table 2). The decrease in the linear growth of the normalized stress of the printed structures indicates an increase in the solid-like behavior with the increase of heating speed. Furthermore, the viscoelastic response decreases with the increase in heating speed and with the decrease in the base material's Young's modulus (Wu et al., 2012). Therefore, by using the in-line heating modulation method, the stress relaxation and viscoelastic response can be modulated throughout the printing process irrespective of the printed relative density.

Finally, the Peleg-Normand parameters were extracted from the slope and intercept (R^2 > 0.98) of the normalized stress profiles averaged over the number of samples ($n = 3$). To elucidate the dependency on the applied NIR heating of the base material, the parameters k_1, k_2, and %SR were plotted against the applied heating speed. As shown in Figure 6a, the %SR increases linearly ($R^2 = 0.99$) with the increase in heating speed or with the decrease in the base material's Young's modulus (Table 2). The %SR was observed to increase from 30.5 ± 0.9% at E_{eng} = 359.3 ± 13.9 kPa to 36.9 ± 3.2% at E_{eng} = 140.8 ± 3.4 kPa. This increase shows a decrease in the solid response with the increase in heating speed (lower heating energy). Which can be contributed to the decrease in mass transfer or moisture loss during heating. While most studies use the Peleg-Normand model for elucidating the stress relaxation behavior of dough, Wu et al. used the Peleg-Normand and %SR constants to study the effect of electric power of steamer on the stress relaxation of steamed breads (Wu et al., 2012). The study showed also an increase in the % SR or the solid response of the foam with respect to the steaming power. As shown in Figure 6a, both k_1 and k_2 constants of the Peleg-Normand model show a linear decrease ($R^2 = 0.99$ and $R^2 = 0.98$, respectively) with different rates in relation to the increase in heating speed. The k_1 constant was observed to decrease from 4.8 ± 0.2 s at E_{eng} = 359.3 ± 13.9 kPa to 3.3 ± 0.3 s at E_{eng} = 140.8 ± 3.4 kPa. Considering the linear decrease in k_1, the behavior indicates a decrease in the initial rate of decay of the compressive stress with the increasing heating speed. This indicates an increase in solid-like behavior and faster stress response which is also confirmed by the increase in %SR at lower applied heating speeds. Moreover, the k_2 constant was

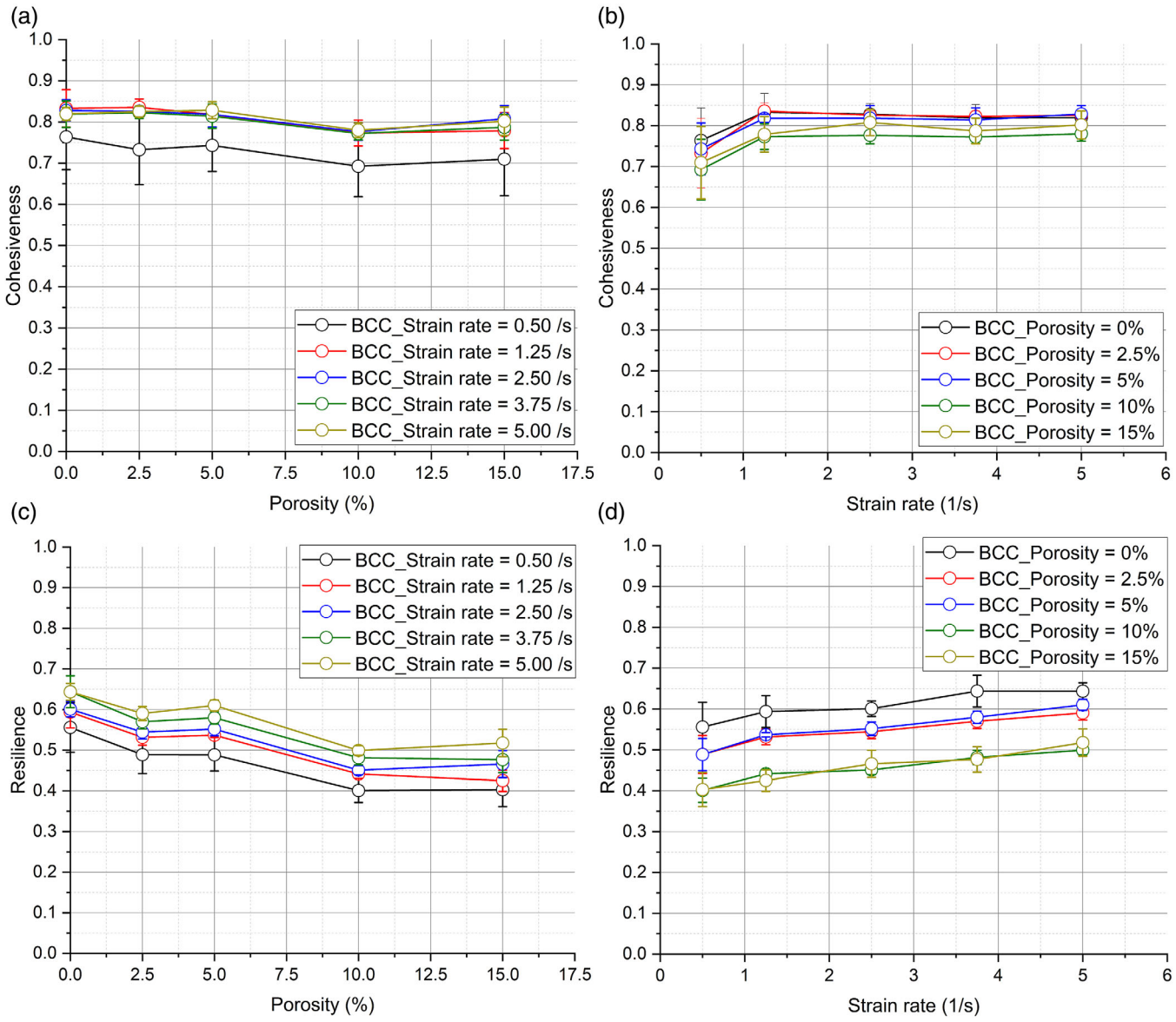

FIGURE 4 TPA measurement of porosity and strain rate dependency of the cohesiveness and resilience of the body-centered cubic (BCC) bubble configuration (STD n = 3): (a) cohesiveness behavior with respect to increasing porosity at different applied strain rates; (b) cohesiveness behavior with respect to increasing strain rate at the designed porosity levels; (c) resilience behavior with respect to increasing porosity at different applied strain rates; (d) resilience behavior with respect to increasing strain rate at the designed porosity levels

observed to decrease from 3.1 ± 0.1 at E_{eng} = 359.3 ± 13.9 kPa to 2.5 ± 0.1 at E_{eng} = 140.8 ± 3.4 kPa. Regarding the linear decrease in k_2, the rate of change is lower than that of the k_1 constant. This behavior indicates a decrease in the residual stress with respect to the decrease in Young's modulus. Finally, the results indicate that at lower heating speeds subjected to the base material, the printed material without porosity tends to possess faster response to relaxation but at the same time the residual stress of the micro-structure increases.

Regarding the dependency of the model coefficients k_1, k_2 and % SR on the closed-cell configurations and porosity levels, they showed primarily the same overall increase or decrease behavior with different decay or growth levels depending on the printed closed-cell configuration. For the SC, BCC, and FCC configurations, the initial rate of decay of the compressive stress k_1 decreases with the increase in structural porosity from 4.8 ± 0.2 s at 0% porosity to 3.1 ± 0.1 s for the SC, to 2.9 ± 0.1 s for the BCC, and to 2.9 ± 0.2 s for the FCC configuration at 15% porosity. The decrease behavior was observed to be different comparing the SC with the BCC and FCC configurations where the SC configuration shows a linear decrease (R^2 = 0.97) while both the BCC and FCC configurations show an exponential decay (R^2 = 0.99). This change of decrease behavior of the BCC and FCC configurations can be contributed to the response of the air bubbles located in the mid-section of the unit cell where the most deformation occurs contrarily to the corner distribution of bubbles in the SC configuration. The overall amount of

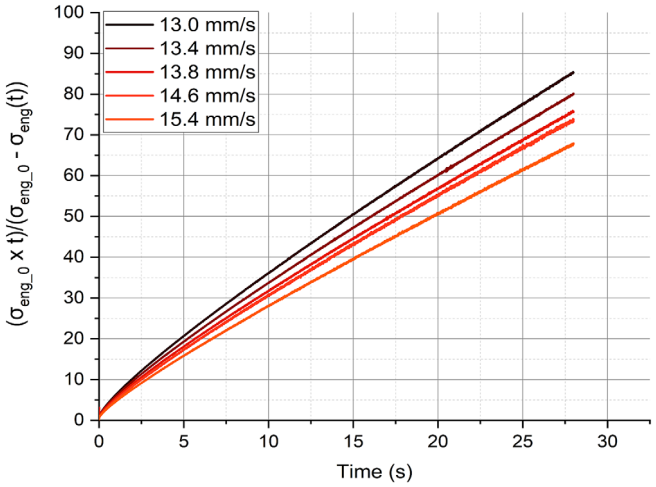

FIGURE 5 Linear regression profiles plotted using the normalized Peleg-Normand stress with respect to the stress relaxation time of the bulk material as a function of applied heating speed

decrease in the rate of decay of compressive stress indicates that the behavior of k_1 is solely dependent on the response of the base material. Regarding the mentioned findings, no literature in food research was found that attempted to study the Peleg-Normand constants in relation to the properties of highly defined pore distributions. Considering the behavior of the residual stress as denoted by k_2 constant, a similar behavior to the k_1 constant was observed. The residual stress constant was observed to decrease linearly with the increase in porosity for the SC, BCC, and FCC configurations. Comparing the dependency on the pore configuration with the dependency on the applied heating speed, it was determined that the behavior of the residual stress is also (similar to k_1) independent of the printed configuration and porosity. Finally, for the three configurations, the %SR increases with the increase in structural porosity from 30.5 ± 0.9% at 0% porosity to 37.4 ± 0.8% for the SC, to 39.4 ± 1.9 s for the BCC, and to 38.2 ± 2.2% for the FCC configuration at 15% porosity. Also, a discrepancy was observed in the increase behavior between the SC with the BCC and FCC configurations where the SC configuration shows a linear increase ($R^2 = 0.99$) while both the BCC and FCC configurations show an exponential growth ($R^2 = 0.99$). The overall amount of increase of %SR is solely dependent on the response of the base material when compared to the change in heating speed. This also indicates that the modulation of the %SR is independent of the printed configuration and porosity.

To characterize the large deformation behavior of the 3D printed closed-cell configurations, the structures were compressed to 80% of their original height. The reaction force was recorded and analyzed against the deformation distance. The engineering stresses and strains were used to analyze the stress–strain curves of the printed structures. Due to the large applied deformations, the true stresses and strains required active real-time monitoring of the sample's deformable surface area which was not possible during this study. Moreover, the obtained engineering stress–strain profiles were fitted with the mentioned Goga PFM (section 2.4).

As shown in Figure 7, the engineering stress–strain profiles were analyzed for the three printed closed-cell configurations at the increasing porosity levels (section 2.3). The illustrated profiles represent as sample of each porosity. All measured profiles show three distinct regions with two transition sites with respect to the stress behavior in relation to the increasing applied strain. The first region (as mentioned in section 2.4) is a linear region where the cell walls of the three configurations bend elastically. Considering the application of small strains (approx. $\epsilon < 0.025$), an exponential increase in stress is observed which can be assumed as an initial densification regime which occurs due to the layer-based approach of 3D printing. This effect can be explained as the initial densification or merging of the layers compressing any gaps which forms during the deposition of layers. Following the linear regime, the first transition period occurs which is the yielding of the internal structure (Gibson, 1989). Yielding occurs at the transition between elastic and plastic deformation of the cell walls where a drop or no increase in stress occurs with the increase in strain (Lu & Abbott, 2004; Roylance, 1996). As shown in Figure 7, the second region which is the plateau regime exists for all configurations in the strain range of approx. ~0.2 till ~0.4. The plateau regime shows a slight increase of stress with respect to the increase in strain for all closed-cell configurations. The increase in stress shows the contribution of air within the cells to the mechanical response of the cellular configurations. As mentioned (Gibson, 1989), closed-cells within cellular foams which are subjected to compression, their volume progressively decreases which increases the air pressure within the cell. This contribution is typical negligible at small strains or to the linear elastic behavior. On the other hand, the increase in air pressure induces a sloping stress plateau in elastomeric foams which can exhibit large deformations without rupture of the cell walls (Gibson, 1989). Thus, as shown in Figure 7, the sloping stress plateau shows that the cells within the printed cellular structures were not subjected to printing induced defects which might transition the closed nature of the cells into a connected network. Following the plateau region, the onset of densification was observed where the exponential strain locking behavior is initiated.

To elucidate the stress–strain behavior of the printed closed-cell configurations, the parameters denoting the damping or yielding coefficients η (kPa), the plateau stiffness E_p (kPa), and the densification coefficients γ (kPa) were extracted from the regression and averaged over the number of samples ($n = 3$). First, the Goga PFM parameters were investigated with respect to the material's modulated Young's modulus at 0% porosity which corresponds to the variable heating speeds (refer to Table 2). Considering the densification coefficient, it remained approx. Constant with respect to the increase of NIR heating speed or to the decrease in Young's modulus, as shown in Figure 8a. The densification coefficient was observed to be an average of 165.4 ± 2.3 kPa. This indicates that the densification regime of the printed structures is independent of the applied heat during 3D printing. In addition, the behavior of the base material during strain locking could be independent of the thermal transitions of the material's constitutive components. This is an indication that the densification behavior is solely dependent of the foam's internal structure and

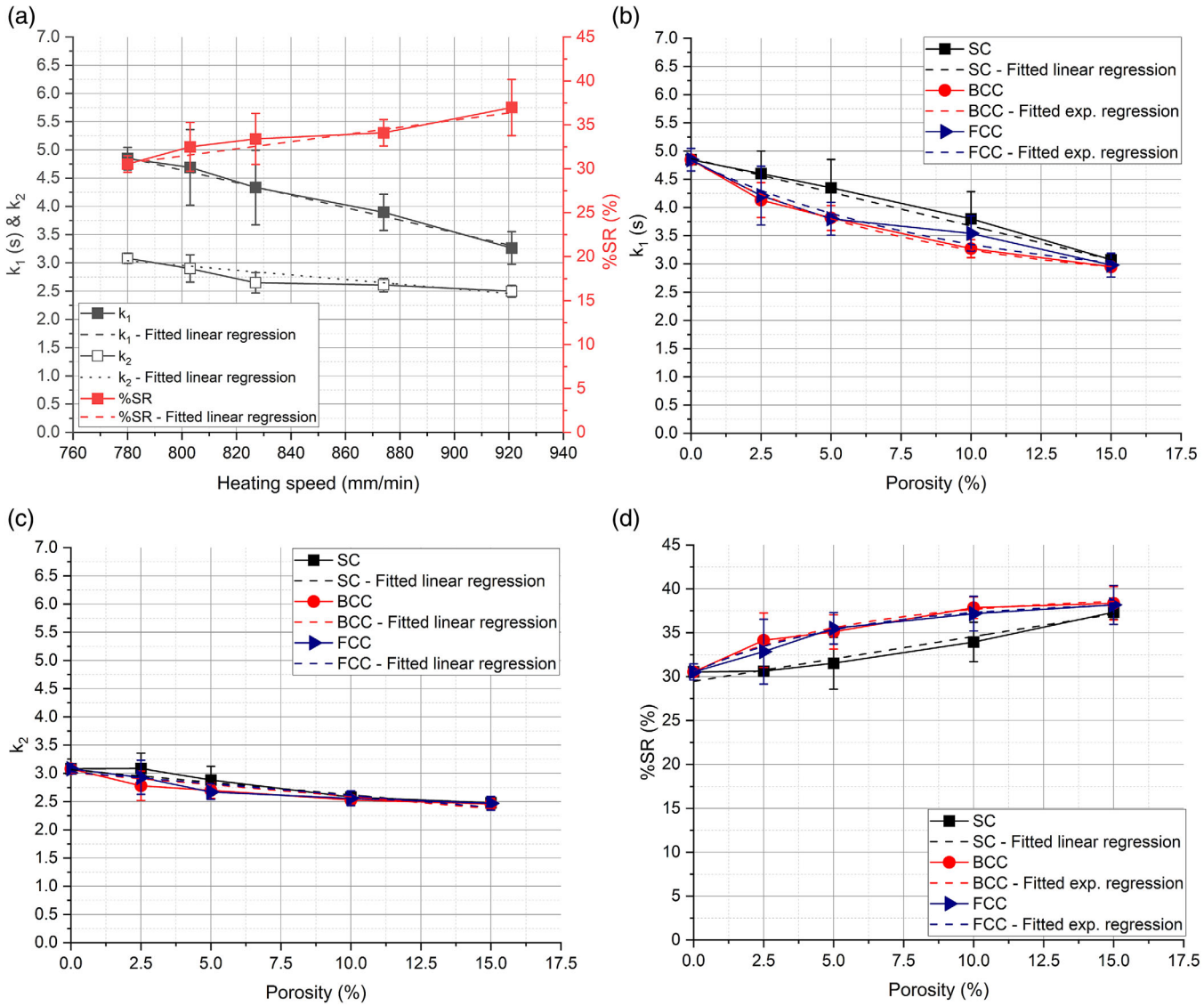

FIGURE 6 Calculated and regression fitted Peleg-Normand model parameters from stress relaxation curves with respect to varying heating speeds and porosities (STD $n = 3$): (a) change in k_1, k_2, and %SR with respect to increasing NIR heating speeds at 0% porosity (base material); (b) behavior of the k_1 intercept at increasing porosity levels for the different 3D printed closed-cell configurations; (c) behavior of k_2 slope at increasing porosity levels for the different 3D printed closed-cell configurations; (d) change in %SR with respect to increasing porosity levels for the different 3D printed closed-cell configurations

relative density. As shown in Figure 8a, unlike the densification coefficient, both the damping and plateau coefficients show an exponential decay behavior with $R^2 = 0.97$ and $R^2 = 0.9$, respectively. This decrease behavior occurs with the increase in NIR heating speed or to the decrease in base material's Young's modulus (refer to Table 2). The damping coefficient which corresponds to the compressive yield stress of the base material was observed to decrease from 44.2 ± 1.9 kPa at $E_{eng} = 359.3 \pm 13.9$ kPa to 22.9 ± 1.1 kPa at $E_{eng} = 140.8 \pm 3.4$ kPa. Thus, the compressive yield stress of the base material can be modulated using the in-line NIR heating system irrespective of the printed porosity or internal structure. Moreover, the plateau coefficient of the base material was observed to decrease from 9.34 ± 0.2 kPa at $E_{eng} = 359.3 \pm 13.9$ kPa to 1.1 ± 0.1 kPa at $E_{eng} = 140.8 \pm 3.4$ kPa. As the plateau regime of cellular foams is correlated with the type or structure of cells (open- or closed-cells) and the enclosed fluid (Gibson, 1989), the change in the plateau stiffness can be contributed to the subjected NIR thermal energy. As the heating speed decreases the heating time of the printed structure increase which increases the occurring mass transfer during NIR thermal stabilization (Dessev et al., 2011; Riadh et al., 2015). Therefore, at lower heating speeds more moisture evaporates which can increase the micro porosity within the printed structures leading to an increase in the plateau response.

Considering the dependency of the model coefficients on the closed-cell configurations and porosity levels, they showed primarily the same behavior with different decay or growth levels depending

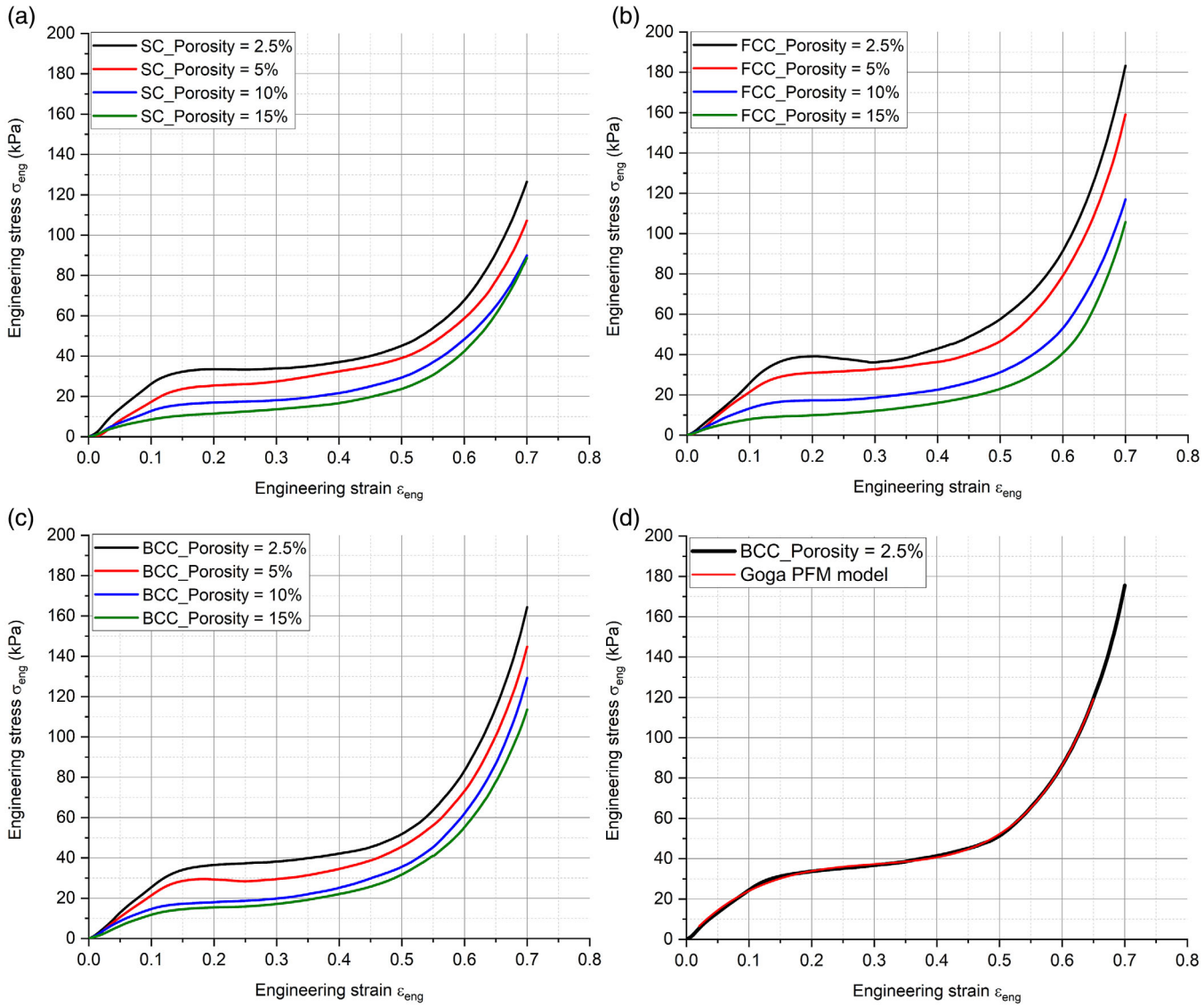

FIGURE 7 Measured engineering stress–strain profiles of the 3D printed closed-cell bubble configurations at the four design porosity levels: (a) engineering stress–strain behavior of SC bubble configuration; (b) engineering stress–strain behavior of FCC bubble configuration; (c) engineering stress–strain behavior of BCC bubble configuration; (d) engineering stress–strain behavior of BCC bubble configuration at 2.5% porosity with Goga PFM regression

on the printed closed-cell configuration. Regarding the damping coefficient or the compressive yield stress of the printed closed-cell configurations, the same exponential decrease as the base material occurs ($R^2_{avg} = 0.98$), as shown in Figure 8b. For the 15% porosity, the three configurations had a compressive yield stress of 16.8 ± 0.6 kPa for the BCC, to 11.9 ± 1.3 kPa for the SC, and to 18.1 ± 2.7 kPa for the FCC configuration. By comparing the results to the yield stress of the base material at the corresponding applied heating speed (22.9 ± 1.1 kPa), it is observed that the inclusion of porosity act as a superposition in the transition between elastic and plastic deformation. The addition of stress concentration points at the cell walls leads to a decrease in the compressive yield stress of the printed structure. Moreover, the lower yield stress of the SC configuration is due to the larger bubbles as for this configuration, the number of cells is lower at the same porosity level.

As shown in Figure 8c, the plateau stiffness showed for the three printed configurations a logarithmic growth behavior with the increase in porosity. This is contributed to the closed-cell response of the air cells to compression which increases with the increase in porosity or amount of compressed air (Gibson, 1989). Illustrated in Figure 8c, the logarithmic growth of the BCC configuration ($R^2 = 0.97$) is observed to be higher than the growth of the SC and FCC configurations ($R^2 = 0.99$ and $R^2 = 0.99$, respectively). The increase in the plateau stiffness of the closed-cell configurations is from 9.34 ± 0.2 kPa at 0% porosity to 47.4 ± 0.2 kPa for the BCC, to 31.3 ± 2.3 kPa for the SC, and to 32.3 ± 5.2 kPa for the FCC configuration. As mentioned in section 2.3, the BCC configuration has a single body-centered bubble while the air bubbles SC and FCC configurations are distributed on the lattice corners and faces. In addition, during compressive testing, the compressive load is not uniform over the

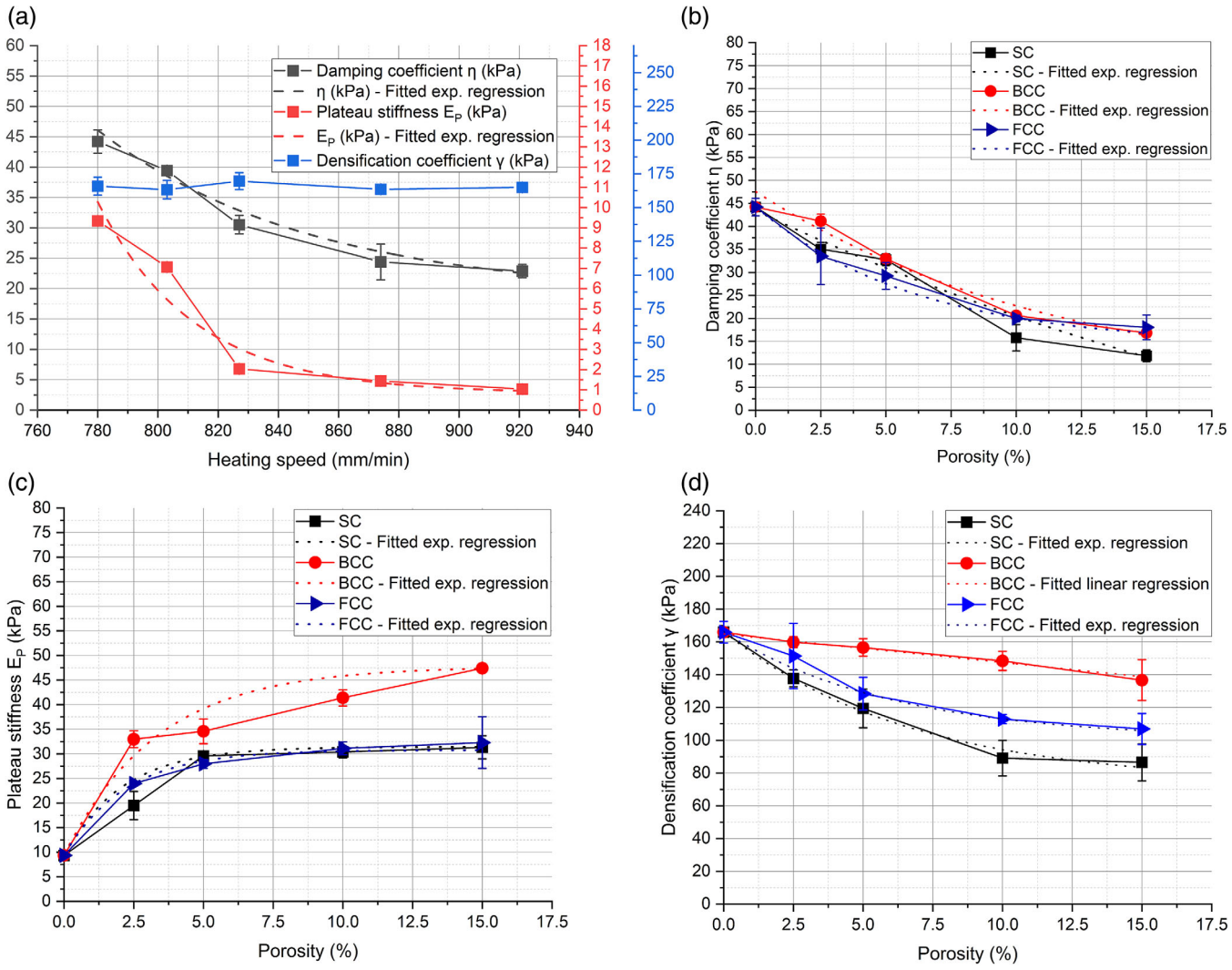

FIGURE 8 Obtained Goga PFM coefficients/stresses from the engineering stress–strain curves with respect to varying heating speeds and porosities (STD $n = 3$): (a) change in damping η, plateau E_P, and densification γ coefficients with respect to increasing NIR heating speeds at 0% porosity (base material); (b) behavior of damping coefficient η with respect to increasing porosity levels of the 3D printed closed-cell bubble configurations; (c) behavior of plateau stiffness E_P with respect to increasing porosity levels of the 3D printed closed-cell bubble configurations; (d) behavior of densification coefficient γ with respect to increasing porosity levels of the 3D printed closed-cell bubble configurations

structure's height. High friction forces act between the top surface and the probe, also high friction forces exist between the bottom surface of the structure and the base support. Thus, low deformation occurs at the structure's top and bottom surfaces (Kramer & Szczesniak, 1973; Peleg, 2019). Therefore, buckling of the middle part occurs which explains the higher registered response of the BCC's centered air bubble.

Considering the densification behavior of the closed-cell configurations, as shown in Figure 8d, a decrease occurs with respect to the increase in porosity. The porosity-modulated behavior is different comparing the BCC configuration with the SC and FCC configurations. The decrease of the densification behavior of the BCC configuration follows a linear regression ($R^2 = 0.99$) while both the SC and FCC configurations follow an exponential decay regression ($R^2 = 0.99$ and $R^2 = 0.99$, respectively). The decrease in the densification coefficient of the closed-cell configurations is from 165.9 ± 6.5 kPa at 0% porosity to 136.6 ± 12.4 kPa for the BCC, to 86.5 ± 11.3 kPa for the SC, and to 106.8 ± 9.4 kPa for the FCC configuration. The results show that the location, size, and number of air bubbles influence the response of the material in the densification regime. Comparing the SC and BCC configurations, the bubble distribution over the lattice structure is the same except for the body-centered bubble of the BCC configuration. As a consequence, the linear decrease behavior of the BCC configuration is caused by the integration of centrally located air cell where the highest deformation occurs during compressive testing. As mentioned before, the behavior of the densification coefficient is independent of the base material's Young's modulus and heating speed. Therefore, the observed decrease behavior shown in Figure 8d proves that the modulation of the densification coefficient occurs through the relative density and the bubble distribution inside the cellular structure.

4 | CONCLUSION

In this study, we extended the texture modulation using 3D printing of starch-based closed-cell foams beyond the elastic regime. We elucidated structure-deformation relations at variable strain rates and large-strain deformation. The main objective was to characterize and understand the behavior of textural properties and stress–strain parameters with respect to the base material's Young's modulus, porosity, and bubble distribution. Three closed-cell configurations were designed printed at five porosity levels. The three closed-cell spherical bubble configurations consisted of simple, base-centered, and face-centered cubic designs. Moisture control and Young's modulus modulation of used starch-based material was performed using in-line NIR thermal stabilization. To verify the precision of the printed structures, hardness levels obtained from FEM simulations and compression analysis were compared and comparable results were achieved.

Concerning the dependency of textural properties on the strain rate of deformation, results showed that the strain rate response of hardness is dependent on the base material's mechanical properties of the cell walls. This is superimposed by the response of the closed cells and porosity which is independent of the printed configuration. Also, the resilience and cohesiveness were observed to be dependent only on the applied strain rate and porosity. The increased response remained unchanged with respect to the applied heating speed and bubble configuration. For characterizing the viscoelastic response of the printed configurations, the stress relaxation spectra were measured, then the Peleg-Normand parameters were evaluated and compared. It was observed for all three configurations that the viscoelastic response is only dependent on the base material properties of the cell walls.

Regarding the stress-stain behavior of the base material, results showed that the densification coefficient remains constant with respect to the increase of NIR heating speed or to the decrease in Young's modulus. The compressive yield stress of the base material can be modulated using the in-line NIR heating system. For the closed-cell configurations, it was observed that the inclusion of porosity act as a superposition in the transition between elastic and plastic deformation. The addition of stress concentration points at the cell walls leads to a decrease in the compressive yield stress of the printed structure. The plateau stiffness showed for the three printed configurations a logarithmic growth behavior with the increase in porosity. This is contributed to the closed-cell response of the air cells to compression. a higher registered response of the BCC's centered air bubble was observed as the compressive load is not uniform over the structure's height. Therefore, buckling of the middle part occurs which explains the higher registered response of the BCC's centered air bubble. Considering the densification behavior, the porosity-modulated behavior was different comparing the BCC configuration with the SC and FCC configurations. The results showed that the location, size, and number of air bubbles influenced the response of the cellular structures in the densification regime.

AUTHOR CONTRIBUTIONS

Ahmed Raouf Fahmy: Methodology; Investigation; Formal analysis; Data curation; Writing - original draft; Visualization; Validation; Software. Mario Jekle: Methodology; Conceptualization; Funding acquisition; Supervision; Writing - review & editing; Project administration; Resources. Thomas Becker: Conceptualization; Writing - review & editing; Funding acquisition; Project administration; Resources.

ACKNOWLEDGMENTS

This research was funded by the Deutsche *Forschungsgemeinschaft* (DFG, German Research Foundation) - 405072578. Open Access funding enabled and organized by Projekt DEAL.

DATA AVAILABILITY STATEMENT

Research data are not shared.

ETHICAL STATEMENTS

Conflict of Interest: The authors declare that they have no known competing financial interests or personal relationships that could have appeared to influence the work reported in this paper or any conflict of interest.

Ethical Review: This study does not involve any human or animal testing.

Informed Consent: Not required.

ORCID

Ahmed Raouf Fahmy https://orcid.org/0000-0003-0218-9380
Mario Jekle https://orcid.org/0000-0002-2560-0040
Thomas Becker https://orcid.org/0000-0001-6842-8300

REFERENCES

Alzoubi, M. F., Abu-Ayyad, M. M., & Al-Hallaj, S. (2014). Modeling of compressiong curves of flexible polyurethane foam with variable density, chemical formulations and strain rates. *Journal of Solid Mechanical*, *6*(1), 82–97.

ASTM-International (2012). Standard terminology for additive manufacturing technologies. In *ASTM F2792-10e1 Standard, Vol ASTM F2792-10e1 Standard*. Pennsylvania: ASTM International.

Attenburrow, G. E., Goodband, R. M., Taylor, L. J., & Lillford, P. J. (1989). Structure, mechanics and texture of a food sponge. *Journal of Cereal Science*, *9*(1), 61–70. https://doi.org/10.1016/S0733-5210(89)80024-4

Avalle, M., Belingardi, G., & Ibba, A. (2007). Mechanical models of cellular solids: Parameters identification from experimental tests. *International Journal of Impact Engineering*, *34*(1), 3–27. https://doi.org/10.1016/j.ijimpeng.2006.06.012

Beer, F. P., Jr., J., E. R., DeWolf, J. T., & Mazurek, D. F. (2011). *Statics and mechanics of materials* (1st ed.). New York: McGraw-Hill.

Chen, J., Mu, T., Goffin, D., Blecker, C., Richard, G., Richel, A., & Haubruge, E. (2019). Application of soy protein isolate and hydrocolloids based mixtures as promising food material in 3D food printing. *Journal of Food Engineering*, *261*, 76–86. https://doi.org/10.1016/j.jfoodeng.2019.03.016

Derossi, A., Caporizzi, R., Oral, M. O., & Severini, C. (2020a). Analyzing the effects of 3D printing process per se on the microstructure and mechanical properties of cereal food products. *Innovative Food Science and Emerging Technologies*, *66*, 102531. https://doi.org/10.1016/j.ifset.2020.102531

Derossi, A., Caporizzi, R., Paolillo, M., & Severini, C. (2020b). Programmable texture properties of cereal-based snack mediated by 3D printing technology. *Journal of Food Engineering*, *289*, 110160. https://doi.org/10.1016/j.jfoodeng.2020.110160

Dessev, T., Jury, V., & Le-Bail, A. (2011). The effect of moisture content on short infrared absorptivity of bread dough. *Journal of Food Engineering*, *104*(4), 571–576. https://doi.org/10.1016/j.jfoodeng.2011.01.019

Fahmy, A. R., Amann, L. S., Dunkel, A., Frank, O., Dawid, C., Hofmann, T., … Jekle, M. (2021a). Sensory design in food 3D printing – Structuring, texture modulation, taste localization, and thermal stabilization. *Innovative Food Science & Emerging Technologies*, *72*, 102743. https://doi.org/10.1016/j.ifset.2021.102743

Fahmy, A. R., Becker, T., & Jekle, M. (2019). *3D printing of starch-based systems: Morphological imaging and flow behavior characterization of multiple stage extrusion through a rheometry imitation approach*. 33rd EFFoST International Conference.

Fahmy, A. R., Becker, T., & Jekle, M. (2020). 3D printing and additive manufacturing of cereal-based materials: Quality analysis of starch-based systems using a camera-based morphological approach. *Innovative Food Science & Emerging Technologies*, *63*(April), 102384. https://doi.org/10.1016/j.ifset.2020.102384

Fahmy, A. R., Becker, T., & Jekle, M. (2021b). *Design and modulation of food textures using 3D printing of closed-cell foams in point lattice systems*. DECHEMA - Jahrestreffen *Lebensmittelverfahrenstechnik*.

Fahmy, A. R., Vogt, U. T., Jekle, M., & Becker, T. (2022). Hardness targeted design and modulation of food textures in the elastic-regime using 3D printing of closed-cell foams in point lattice systems. *Journal of Food Engineering*, *320*, 110942. https://doi.org/10.1016/j.jfoodeng.2022.110942

Gao, J., Wang, Y., Dong, Z., & Zhou, W. (2018). Structural and mechanical characteristics of bread and their impact on oral processing: A review. *International Journal of Food Science and Technology*, *53*(4), 858–872. https://doi.org/10.1111/ijfs.13671

Gholamipour-Shirazi, A., Kamlow, M. A., Norton, I. T., & Mills, T. (2020). How to formulate for structure and texture via medium of additive manufacturing-a review. *Foods*, *9*(4), 497. https://doi.org/10.3390/foods9040497

Gibson, L. J. (1989). Modelling the mechanical behavior of cellular materials. *Materials Science and Engineering A*, *110*, 1–36. https://doi.org/10.1016/0921-5093(89)90154-8

Gibson, L. J., & Ashby, M. F. (1999). *Cellular-solids-structure-and-properties-cambridge-solid-state-science-series-.pdf*. (p. 510).

Godoi, F. C., Prakash, S., & Bhandari, B. R. (2016). 3d printing technologies applied for food design: Status and prospects. *Journal of Food Engineering*, *179*, 44–54. https://doi.org/10.1016/j.jfoodeng.2016.01.025

Goga, V., & Hučko, B. (2016). Phenomenological material model of foam solids. *Strojnícky Casopis – Journal of. Mechanical Engineering*, *65*(1), 5–20. https://doi.org/10.1515/scjme-2016-0001

Hatcher, D. W., Bellido, G. G., Dexter, J. E., Anderson, M. J., & Fu, B. X. (2008). Investigation of uniaxial stress relaxation parameters to characterize the texture of yellow alkaline noodles made from durum and common wheats. *Journal of Texture Studies*, *39*(6), 695–708. https://doi.org/10.1111/j.1745-4603.2008.00164.x

Jang, W., Kraynik, A. M., & Kyriakides, S. (2008). On the Microstructure of Open-Cell Foams and its Effect on Elastic Properties. *International Journal of Solids and Structures*, *45*, 1845–1875. https://doi.org/10.1016/j.ijsolstr.2007.10.008

Jonkers, N., van Dommelen, J. A. W., & Geers, M. G. D. (2020). Experimental characterization and modeling of the mechanical behavior of brittle 3D printed food. *Journal of Food Engineering*, *278*, 109941. https://doi.org/10.1016/j.jfoodeng.2020.109941

Kramer, A., & Szczesniak, A. S. (Eds.). (1973). *Texture measurement of foods* (1st ed.). Netherlands: Springer. https://doi.org/10.1007/978-94-010-2562-1

Lille, M., Kortekangas, A., Heiniö, R. L., & Sozer, N. (2020). Structural and textural characteristics of 3D-printed protein- and dietary fibre-rich snacks made of milk powder and wholegrain rye flour. *Foods*, *9*(11), 1527. https://doi.org/10.3390/foods9111527

Lipton, J., Arnold, D., Nigl, F., Lopez, N., Cohen, D., Norén, N., & Lipson, H. (2010). Mutli-material food printing with complex internal structure suitable for conventional post-processing. *21st annual international solid freeform fabrication symposium - an additive manufacturing conference, SFF 2010*. (January 2010. pp. 809–815).

Liu, Q., & Subhash, G. (2004). A phenomenological constitutive model for foams under large deformations. *Polymer Engineering and Science*, *44*(3), 463–473. https://doi.org/10.1002/pen.20041

Liu, Z., Bhandari, B., Prakash, S., & Zhang, M. (2018). Creation of internal structure of mashed potato construct by 3D printing and its textural properties. *Food Research International*, *111*(2017), 534–543. https://doi.org/10.1016/j.foodres.2018.05.075

Liu, Z., & Zhang, M. (2021). Texture properties of microwave post-processed 3D printed potato snack with different ingredients and infill structure. *Future Foods*, *3*, 100017. https://doi.org/10.1016/j.fufo.2021.100017

Lu, R., & Abbott, J. A. (2004). Force/deformation techniques for measuring texture. In *Texture in food* (Vol. 2, pp. 109–145). Amsterdam: Elsevier Inc. https://doi.org/10.1533/978185538362.2.109

Mantihal, S., Kobun, R., & Lee, B. B. (2020). 3D food printing of as the new way of preparing food: A review. *International Journal of Gastronomy and Food Science*, *22*, 100260. https://doi.org/10.1016/j.ijgfs.2020.100260

Peleg, M. (2019). The instrumental texture profile analysis revisited. *Journal of Texture Studies*, *50*(5), 362–368. https://doi.org/10.1111/jtxs.12392

Peleg, M., & Normand, M. D. (1983). Comparison of two methods for stress relaxation data presentation of solid foods. *Rheologica Acta*, *22*(1), 108–113. https://doi.org/10.1007/BF01679835

Pereira, T., Barroso, S., & Gil, M. M. (2021). Food texture design by 3D printing: A review. *Foods*, *10*(2), 320. https://doi.org/10.3390/foods10020320

Phuhongsung, P., Zhang, M., & Devahastin, S. (2020). Influence of surface pH on color, texture and flavor of 3D printed composite mixture of soy protein isolate, pumpkin, and beetroot. *Food and Bioprocess Technology*, *13*(9), 1600–1610. https://doi.org/10.1007/s11947-020-02497-8

Piovesan, A., Vancauwenberghe, V., Aregawi, W., Delele, M. A., Bongaers, E., de Schipper, M., … Nicolai, B. (2020). Designing mechanical properties of 3D printed cookies through computer aided engineering. *Foods*, *9*(12), 1804. https://doi.org/10.3390/foods9121804

Riadh, M. H., Ahmad, S. A. B., Marhaban, M. H., & Soh, A. C. (2015). Infrared heating in food drying: An overview. *Drying Technology*, *33*(3), 322–335. https://doi.org/10.1080/07373937.2014.951124

Roylance, D. (1996). *Mechanics of materials* (1st ed.). New York, NJ: Wiley & Sons.

Shahbazi, M., Jäger, H., & Ettelaie, R. (2021a). Application of Pickering emulsions in 3D printing of personalized nutrition. Part I: Development of reduced-fat printable casein-based ink. *Colloids and Surfaces A: Physicochemical and Engineering Aspects*, *622*, 126641. https://doi.org/10.1016/j.colsurfa.2021.126641

Shahbazi, M., Jäger, H., & Ettelaie, R. (2021b). Application of Pickering emulsions in 3D printing of personalized nutrition. Part II: Functional properties of reduced-fat 3D printed cheese analogues. *Colloids and Surfaces A: Physicochemical and Engineering Aspects*, *624*, 126760. https://doi.org/10.1016/j.colsurfa.2021.126760

Sun, J., Peng, Z., Zhou, W., Fuh, J. Y. H., Hong, G. S., & Chiu, A. (2015a). A review on 3D printing for customized food fabrication. *Procedia Manufacturing*, *1*, 308–319. https://doi.org/10.1016/j.promfg.2015.09.057

Sun, J., Zhou, W., Huang, D., Fuh, J. Y. H., & Hong, G. S. (2015b). An overview of 3D printing Technologies for Food Fabrication. *Food and Bioprocess Technology*, *8*(8), 1605–1615. https://doi.org/10.1007/s11947-015-1528-6

Szczesniak, A. S. (1963). Classification of textural characteristics. *Journal of Food Science*, *28*, 385–389.

Szczesniak, A. S. (2002). Texture is a sensory property. *Food Quality and Preference*, *13*(4), 215–225. https://doi.org/10.1016/S0950-3293(01)00039-8

Takahashi, T., Hayakawa, F., Kumagai, M., Akiyama, Y., & Kohyama, K. (2009). Relations among mechanical properties, human bite parameters, and ease of chewing of solid foods with various textures. *Journal of Food Engineering*, *95*(3), 400–409. https://doi.org/10.1016/j.jfoodeng.2009.05.023

Vancauwenberghe, V., Mbong, V. B. M., Vanstreels, E., Verboven, P., Lammertyn, J., & Nicolai, B. (2019). 3D printing of plant tissue for innovative food manufacturing: Encapsulation of alive plant cells into pectin based bio-ink. *Journal of Food Engineering*, *263*, 454–464. https://doi.org/10.1016/j.jfoodeng.2017.12.003

Vancauwenberghe, V., Verboven, P., Lammertyn, J., & Nicolaï, B. (2018). Development of a coaxial extrusion deposition for 3D printing of customizable pectin-based food simulant. *Journal of Food Engineering*, *225*, 42–52. https://doi.org/10.1016/j.jfoodeng.2018.01.008

Varghese, C., Wolodko, J., Chen, L., Doschak, M., Srivastav, P. P., & Roopesh, M. S. (2020). Influence of selected product and process parameters on microstructure, rheological, and textural properties of 3D printed cookies. *Foods*, *9*(7), 907. https://doi.org/10.3390/foods9070907

Wang, S., Austin, P., & Bell, S. (2011). It's a maze: The pore structure of bread crumbs. *Journal of Cereal Science*, *54*(2), 203–210. https://doi.org/10.1016/j.jcs.2011.05.004

Wegrzyn, T. F., Golding, M., & Archer, R. H. (2012). Food layered manufacture: A new process for constructing solid foods. *Trends in Food Science and Technology*, *27*(2), 66–72.

Wu, M. Y., Chang, Y. H., Shiau, S. Y., & Chen, C. C. (2012). Rheology of fiber-enriched steamed bread: Stress relaxation and texture profile analysis. *Journal of Food and Drug Analysis*, *20*(1), 133–142. https://doi.org/10.38212/2224-6614.2083

Zghal, M. C., Scanlon, M. G., & Sapirstein, H. D. (2002). Cellular structure of bread crumb and its influence on mechanical properties. *Journal of Cereal Science*, *36*(2), 167–176. https://doi.org/10.1006/jcrs.2001.0445

Zhao, Z., Wang, Q., Yan, B., Gao, W., Jiao, X., Huang, J., … Fan, D. (2021). Synergistic effect of microwave 3D print and transglutaminase on the self-gelation of surimi during printing. *Innovative Food Science and Emerging Technologies*, *67*, 102546. https://doi.org/10.1016/j.ifset.2020.102546

Zhu, S., Vazquez, I., de Azua, R., Feijen, S., Jan, A., der Goot, V., … Stieger, M. (2021). How macroscopic structure of 3D printed protein bars filled with chocolate influences instrumental and sensory texture. *LWT*, *151*, 112155. https://doi.org/10.1016/j.lwt.2021.112155

How to cite this article: Fahmy, A. R., Jekle, M., & Becker, T. (2023). Texture modulation of starch-based closed-cell foams using 3D printing: Deformation behavior beyond the elastic regime. *Journal of Texture Studies*, *54*(1), 153–169. https://doi.org/10.1111/jtxs.12729